

# Reproducing a Talbot Effect Wavemeter

Jade Chongsathapornpong

*MIT Department of Physics, 77 Massachusetts Ave., Cambridge, MA 02139*

(Dated: May 14, 2024)

Establishing the wavelength of a light source is a common prerequisite in applications such as laser spectroscopy experiments and laser cooling. Modern wavelength meters provide precise and accurate measurements, but are typically expensive. This project sought to reproduce a low-cost Talbot effect wavemeter, and then produce documentation for others seeking to replicate the device themselves. Unfortunately, this effort failed to produce useful results. Here we outline the theory of the Talbot wavemeter, detail simulations not given in the original publications, and describe the key issues preventing our prototype from returning sufficiently accurate and consistent results. The goal is for a non-expert hobbyist reading this document to be able to retrace the steps, especially of the methods section.

**Code and CAD:** <https://github.com/Certaingemstone/OpenQuantum>  
under teaching/mit-spring-2024/experiment/talbot-wavemeter

## I. INTRODUCTION

With broadening interest in quantum engineering and experiment, there is a need to make hardware and instruments more accessible. Among citizen scientists and throughout secondary education, people who might otherwise be interested in practical experience with quantum hardware face a major cost barrier to entry. Lowering the cost of instrumentation could strengthen the ranks of professional researchers by expanding the body of people with early-career exposure to the field. The OpenQuantum project seeks relatively low-cost quantum devices using 3D-printed and common commercial off-the-shelf components, with publicly available specifications. Currently, OpenQuantum is developing a sub-\$5000 rubidium magneto-optical trap to enable exploration of cold atom physics. A coarse measurement of laser wavelength, as provided by a wavelength meter, would be useful for initialization of the requisite frequency-stabilized laser source.

Professional interferometric wavemeters can be costly, from  $\$10^3$  to  $\$10^5$ . In 2019, Han et al. developed a low-cost wavemeter with 10pm resolution using Talbot interferograms and tone parameter estimation algorithms [1]. The same device, consisting of a beam expander, wavelength-scale transmission grating, and a tilted monochrome image sensor sampling the Talbot pattern following the grating, can serve as a transform spectrometer with nm resolution in the visible range [2]. The device no longer exists and, critically, its design, its simulation and data analysis software, and its usage instructions were not documented for reproduction.

In this project, we investigated the device premise by simulating imaging of a Talbot pattern under different sensor, grating, and beam incidence conditions. We constructed a prototype Talbot wavemeter following the description from the publications, illuminated it with different laser sources, and then used a bandpass filter followed by a direct row-wise Fourier transform to produce an output signal from acquired images.

Unfortunately, several issues remain: artifacts and fixed patterns in the output of our color CMOS sensor at scales similar to the Talbot features of interest, the difficulty of manual alignment and identifying an aligned configuration, and the sensitivity of output to alignment and geometric factors. Some issues may be resolved by modifications or clever engineering, and so this report provides example components and setup considerations, alongside accompanying FreeCAD files and example code sufficient for a hobbyist to explore the project themselves.

## II. THEORY

The Talbot effect is observed when plane waves interact with a periodic structure. In our case, this is coherent light incident on a diffraction grating. It is a consequence of interference between different orders of diffracted waves, which propagate at different angles to the structure. In the near-field, where multiple diffracted waves are present, the interference leads to periodic self-imaging of the structure—the Talbot effect. The periodicity of the Talbot self-images is related to the wavelength of the light and the periodicity of the grating. Therefore, by acquiring the Talbot pattern one can in principle estimate the wavelength which produced it.

### A. Non-paraxial limit of the Talbot effect

The periodicity of the Talbot self-images was derived by Rayleigh in the 1880s. Consider a transmission grating with periodicity  $d$ , with a plane wave of wavelength  $\lambda$  incident on its normal. Let the  $x$ -direction be the direction of periodicity of the grating, and the  $z$  direction be the grating normal. The resulting diffracted beams of order  $m$  propagate in different directions, at angles  $\theta_m$  relative to the grating's normal, approximately by the

generalized grating equation,

$$\sin \theta_0 + \sin \theta_m = \frac{m\lambda}{d \sin \gamma} \quad (1)$$

where  $\theta_0$  is the angle of incidence relative to the grating normal in the  $x-z$  plane, and  $\gamma$  is the angle between the direction of incidence and the  $y$  direction. We will use this in later simulations. For normal incidence,  $\gamma = \pi/2$  and  $\theta_0 = 0$ , so Eq. 1 reduces to the commonly known condition,

$$\sin \theta_m = \frac{m\lambda}{d} \quad (2)$$

Using this, one can write an expression for a superposition of amplitudes of diffracted plane waves for an infinite grating, taking the wavenumber  $k = 2\pi/\lambda$ ,

$$\begin{aligned} & A_0 \cos(kz) + A_1 \cos\left(\frac{2\pi x}{d}\right) \cos(\mu_1 z) \\ & - A_{-1} \cos\left(\frac{2\pi x}{d}\right) \sin(\mu_1 z) + A_2 \cos\left(\frac{4\pi x}{d}\right) \cos(\mu_2 z) \\ & - A_{-2} \cos\left(\frac{4\pi x}{d}\right) \sin(\mu_2 z) + \dots \end{aligned} \quad (3)$$

where  $A_m$  are the amplitudes of the diffracted beams. This series continues as long as  $\mu_m$  are real,

$$\mu_m^2 = k^2 - \frac{4\pi^2 m^2}{d^2} = 4\pi^2 \left( \frac{1}{\lambda^2} - \frac{m^2}{d^2} \right) \quad (4)$$

The Talbot self-images faithfully reproduce the generating periodic structure when many  $m$ -th order diffracted waves overlap, that is, when  $\lambda^2 \ll d^2$  and the diffraction angles are small. This is known as the paraxial limit, shown in Fig. 2. However, in the non-paraxial limit when  $\lambda \approx d$ , the vast majority of diffracted power lies in the  $m = 0$  and  $m = \pm 1$  beams. Truncating the amplitude series accordingly and squaring to obtain intensities yields a function periodic in the  $x-z$  plane with period in  $z$  given by

$$z_T = \frac{\lambda}{1 - \sqrt{1 - \frac{\lambda^2}{d^2}}} \quad (5)$$

where  $z_T$  is referred to as the Talbot length [3].

Notably, the generalized grating equation Eq. 1 is exact for  $\gamma = \pi/2$  only; the wavevectors of the diffracted beams are non-coplanar for  $\gamma \neq \pi/2$ , instead falling on an arc including the  $m = 0$  transmitted beam, as shown in Fig. 1. This creates an intensity which is a function of  $x$ ,  $y$ , and  $z$ , instead of only  $x$  and  $z$  [4].

### B. Wavelength determination by imaging a non-paraxial Talbot pattern

The  $z_T$  determines  $\lambda$  from  $d$ . Inverting Eq. 5 yields

$$\lambda = \frac{2z_T d^2}{z_T^2 + d^2} \quad (6)$$

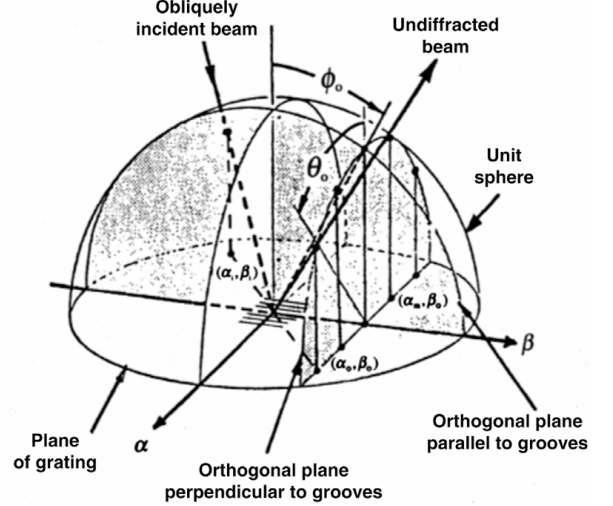


FIG. 1: Real-space directions and their cosine projections on the plane, for diffracted beams from a reflection grating under oblique incidence,  $\gamma \neq \pi/2$  i.e.  $\phi_0 \neq 0$  in this diagram's coordinate system. The result is similar for transmission gratings. Notice for  $\phi_0 \neq 0$  the directions are not coplanar. From [4].

The strategy of [1] is to tilt an image sensor by  $\theta_s$  away from to the grating, around the  $x$  axis (direction of periodicity), as depicted in Fig. 3. This allows photosites to sample different values of  $z$ , keeping  $x$  constant along a given column, meaning that each column captures the  $z_T$  periodic intensity. The roughly square photosites are spaced center-to-center by the pixel pitch  $z_{\text{pix}}$ , and so the sample spacing in the  $z$  direction is simply

$$\Delta z = z_{\text{pix}} \sin \theta_s \quad (7)$$

From the images, one can extract  $z_T$ . Notably, if the image sensor is instead tilted around the  $y$  axis, the resulting image is less directly useful.

### C. Considerations on sensor pixel pitch

For operation in the non-paraxial limit for UV-Vis-NIR light, the spacing between pixels  $z_{\text{pix}}$  is similar to  $z_T$ . The tilt angle  $\theta_s$  is therefore bounded from above such that the sampling of the Talbot pattern  $\Delta z$  is sufficiently fine to avoid the Nyquist limit. Moreover, the sensor must remain within the zone where the multiple diffracted waves are present. On the other hand, to achieve higher resolutions requires sampling many cycles of the Talbot pattern, so a higher  $\theta_s$  is preferred. Additionally, the periodicity of the grating required is typically smaller than  $z_{\text{pix}}$ , meaning that to avoid aliasing,  $z_{\text{pix}}$  should not be a multiple of the grating period [2].

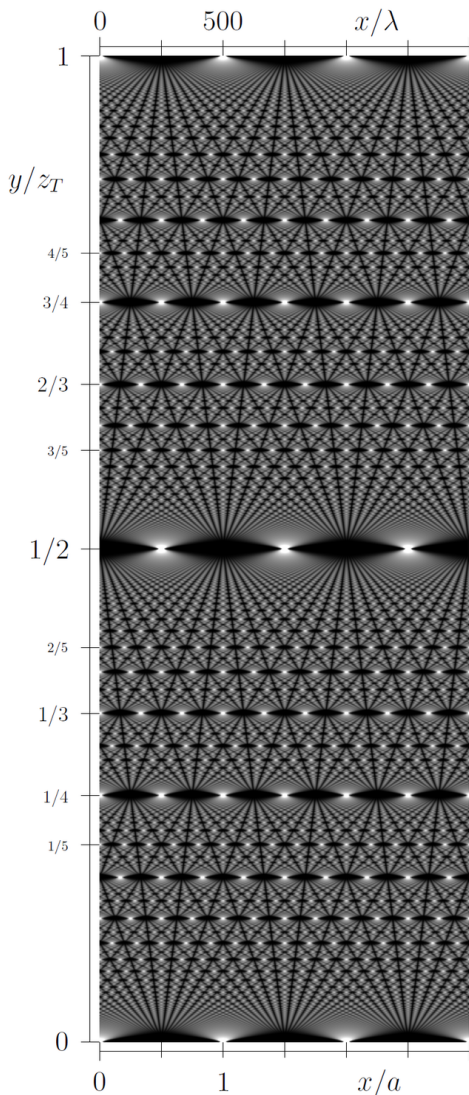


FIG. 2: A Talbot carpet. Structure on the horizontal and space after the structure measured in fractions of Talbot length  $z_T$  on the vertical axis. From Wikimedia Commons.

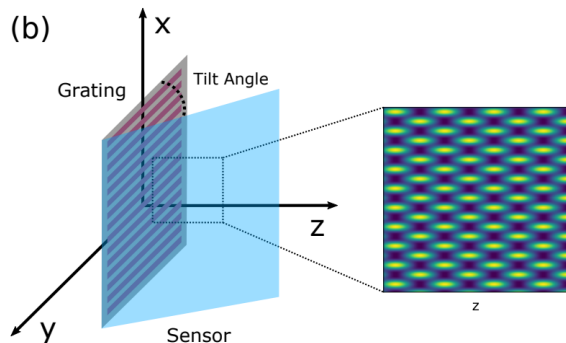


FIG. 3: Diagram of the sensor-grating arrangement, from [1]. The sensor samples the pattern periodic in  $x$  and  $z$ .

### III. IMAGING SIMULATIONS

To get some intuition for the system, we acquired simulated images by sampling the non-paraxial Talbot patterns at a plane of points, then downsampling to simulate the finite size of a pixel. Each pixel summed intensities over a grid of points, evenly spaced.

These calculations were done for normal incidence using an expression for the intensity provided by [5]. To characterize the effects of *non-normal* incidence, which were not clearly described in publications, we additionally produce the corresponding expression with two additional degrees of freedom using Eq. 1. For  $\gamma \neq \pi/2$  we neglect the additional  $y$ -dependence and non-coplanar directions of diffracted beams not captured in Eq. 1. Neglecting the  $y$ -dependence is also inaccurate because the direction of periodicity of the Talbot pattern will follow the direction of the incident beam /  $m = 0$  transmitted beam. However, for small change in  $\gamma$  we can imagine the effect we are missing as an effective change in the sensor tilt angle  $\theta_s$ , equal to the change in  $\gamma$ . This is apparent cross-referencing Fig. 3 and Fig. 1.

The simulations can be run in the `3planewaves.ipynb` Jupyter notebook.

#### A. Modeling the intensity field

For normal incidence, the intensity takes the form

$$I(x, z) \propto A_0^2 + A_1^2 + A_{-1}^2 + 2A_1A_{-1} \cos(4\pi x/d) + 2A_0(A_1 + A_{-1}) \cos(2\pi x/d) \cos(2\pi z/z_T) + 2A_0(A_1 - A_{-1}) \sin(2\pi x/d) \sin(2\pi z/z_T) \quad (8)$$

according to [5].

In non-normal incidence described by angles  $\theta_0$  and  $\gamma$ , we need to recompute the amplitudes resulting from interference of the three ( $m = 0$  and  $m = \pm 1$ ) plane waves propagating in directions  $\theta_m$  determined by Eq. 1. The result is analogous to the expression Eq. 3 describing the normal incidence case. The imaging simulation then samples the intensity, i.e. squared interfered amplitudes.

#### B. Effects of perturbations

Using the model, we study the effects of matching  $z_{\text{pix}}$  to  $d$ , sensor rotation, and non-normal incidence on the grating. All calculations were done assuming a  $1.2\mu\text{m}$  grating periodicity, and a  $50 \times 2400$  pixel sensor with  $1.12\mu\text{m}$   $z_{\text{pix}}$ . The sensor was tilted  $20^\circ$ . Each pixel sampled a  $5 \times 5$  grid. All figures here are  $50 \times 50$  crops of the resulting images.

Fourier transforms were performed along the rows. With perfectly normal incidence and perfect sensor alignment, the resulting image is an interpenetrating rectangular lattice of ellipse-like spots, as shown in Fig. 3.

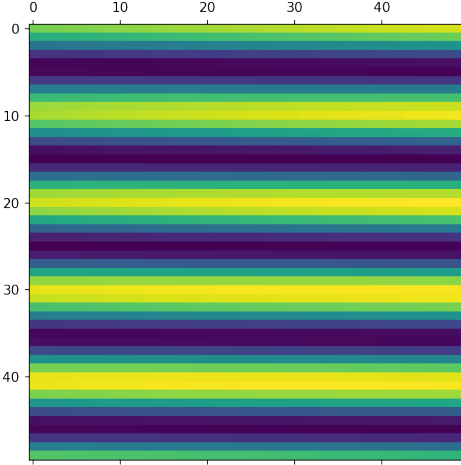


FIG. 4: Image from pixel pitch being a multiple (4x) the grating periodicity, with the sensor slightly shifted in the  $x$ -direction. If not for the shift, the imaged pattern is constant in  $x$ . This effect destroys the  $z_T$  determination according to [2]. This was usually, but not always, the case in our simulations.

First, the pixel pitch was adjusted to be a multiple of the grating periodicity, which [2] claims destroys the Talbot pattern's  $z$ -periodicity. According to the model provided by [5] this is not the case; the  $z$ -periodicity of the image of the pattern is preserved, and it is the  $x$ -periodicity that is destroyed by aliasing. This is shown in Fig. 4. However, from the intensity model by [5], the  $z_T$  and wavelength is still sometimes determined correctly by Fourier transform of the resulting image—except under most translations and rotations of the sensor. Our three plane wave model agrees. It is thus advisable to follow the pixel-grating matching condition, where the pixel pitch is near an odd multiple of half the grating periodicity. Moving off this condition smears the Talbot pattern.

Next, the sensor was rotated about its normal before being tilted. In the image, this manifests as a shearing of the checkerboard pattern of otherwise ellipse-like peaks, shown for the extreme  $5^\circ$  case in Fig. 6. This results in the formation of two spatial frequencies in its rows, splitting off from the true  $z_T$ . The splitting grows sharply with rotation angle—a  $1^\circ$  rotation yields an asymmetric splitting of over 200nm on the 632nm true wavelength according to the model from [5], but this splitting is significantly weaker in our model using three plane waves. A more realistic  $0.1^\circ$  rotation splits the peaks by tens of nanometers, fairly symmetrically, as shown in Fig. 5.

Finally, we explored the effects of non-normal incidence. It is worth noting that our three plane wave model does not seem to reproduce the intensity described by [5] when  $\gamma = \pi/2$  and  $\theta_0 = 0$ . Additionally, our model seems to produce a handful of peaks in the Fourier transform besides the main  $z_T$  peak. This merits further investiga-

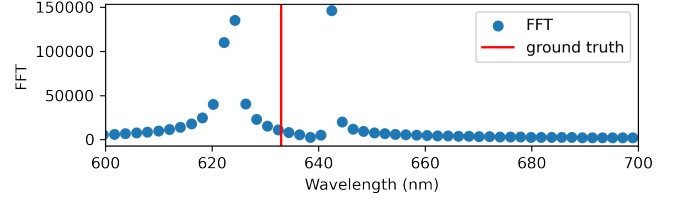


FIG. 5: Fourier transform extraction of wavelength from image from  $0.1^\circ$  rotation of sensor about its normal. True wavelength in red line.

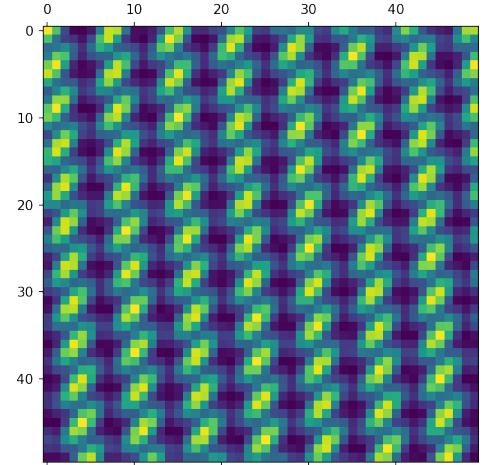


FIG. 6: Image from sensor rotation by 5 degrees, according to the model from [5]. The Talbot peaks are sheared.

tion, however, the patterns look qualitatively similar.

After setting some small realistic perturbations to the sensor ( $x$  shift of 0.11 pixels, rotation of  $0.01^\circ$ ), we tuned up  $\theta_0$ . The effect of  $\gamma$  is relatively small *in this approximation*, though as mentioned earlier, it must lead to a change in the effective sensor tilt angle, which would shift all wavelengths significantly.

Changing  $\theta_0$  also applies a sort of shear transformation to the observed pattern. For small values, the main Talbot peak splits, as shown in Fig. 7. According to our model, many new peaks would form far away. However, at large  $\theta_0$ , a slightly shifted peak may reform where the peak from normal incidence was, seen in Fig. 8.

In all, the observed interference pattern appears extremely sensitive to perturbed geometries and alignment, which is not promising for a robust instrument. Additionally, at least our three plane wave model suggests spurious FFT peaks may form, which would make calibration difficult. Based on our modeling, the goal in alignment is to produce a grid of Talbot peaks axis-aligned to the sensor, as in Fig. 3. Because perturbations in beam incidence and sensor rotation look similar, it is likely difficult



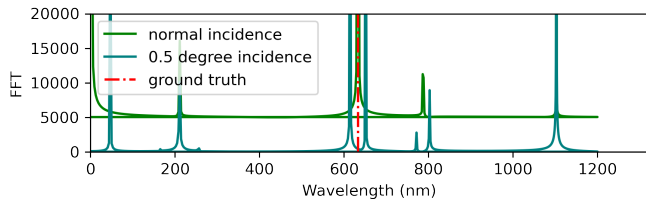


FIG. 7: The wavelengths deduced by FFT of interference of three plane waves from oblique incidence at  $0.5^\circ$ , compared to normal incidence. Note the peak splitting.

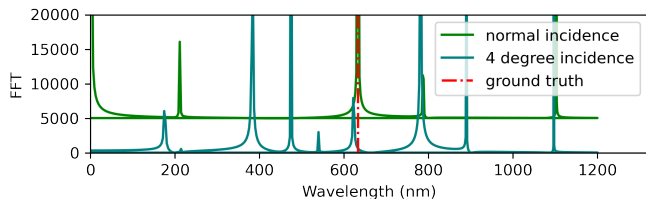


FIG. 8: Same as Fig. 7 but at  $4^\circ$ . Note a slightly shifted peak reforms near where the true peak is supposed to be, and new peaks not found at  $0.5^\circ$ .

to achieve.

## IV. METHODS

Now, we describe the construction and evaluation of our Talbot wavemeter.

### A. Constructing the wavemeter

The device was constructed by 3D printing a mount in PLA. It had two parts fitted with M3 heat-set inserts. A  $1/2$ " square diffraction grating (830 line/mm, period 1.2 $\mu$ m) slid into one part (`GratingSensorMount`) and was held in place by 0.3mm pockets on the sides, then clamped by the other part (`GratingClamp`). The first part provides a mounting plane for a circuit board tilted at an angle, so the sensor falls within 10mm of the grating surface. Care is taken to match the geometry, particularly the orientation of the grating, to Fig. 3. Care must also be taken to ensure the sensor is not rotated around its normal relative to the grating, as this leads to a splitting of the computed  $z_T$  peaks described in Section III B. The sensor used is any high-resolution CMOS or CCD sensor in roughly  $1/2.8$ " format, subject to Section II C. In our case, it is a color 16MP Sony IMX298 (1.12 $\mu$ m  $z_{\text{pix}}$ ) on a breakout board provided by Arducam—this is a bad choice as  $1.12 \approx 1.2\mu$ m of the grating. Our modeling suggests that this reduces visibility. Preferably, the sensor is monochrome—otherwise, debayering artifacts cause issues—but we did not have this option.

### B. Apparatus and alignment

All components were mounted on an optical breadboard. A 30mW 632.8nm HeNe laser was used as reference, as its wavelength is well-defined. The beam was first passed through an OD2 neutral density filter, to avoid saturating the sensor. A generic 8X beam expander from eBay which happened to be longpassed around 500nm was mounted in a V clamp. The wavemeter was mounted about 20" from its output on a 1" kinematic lens mount. After initial alignment, the laser and beam expander were adjusted until the expanded beam fell on the wavemeter input. Taping over the input port helped visualize the beam. Then, further adjustments were made until the laser additionally entered and exited the beam expander perceptually at the centers of the corresponding elements, determined by taking orthogonal views. Finally, approximately normal incidence was sought by tuning the wavemeter kinematic mount. The original publications did not specify how to confirm normal incidence, but from simulations we deduced this at the end of Section III B.

### C. Processing wavemeter images

Extraction of the Talbot length  $z_T$  from images is performed by first applying difference-of-Gaussians as a bandpass filter, selecting for feature sizes of interest ( $z_T$  projected onto the sensor plane) and rejecting slowly varying background. Then, the rows are zero-padded to accommodate fast discrete Fourier transform algorithms and sinc-interpolate the resulting FFT points. Finally, row-wise FFT returns the frequency components in units of inverse  $\Delta z$ , which are rescaled by  $\Delta z$  to obtain the corresponding  $z_T$  and therefore  $\lambda$ .

During alignment, one can observe the output image, apply the bandpass filter, and view the Fourier transform of image rows using `live.py`, which depends on `OpenCV`, `scikit-image`, `numpy`, and `matplotlib`. Images can also be captured using software of choice and processed offline in the `analysis.ipynb` Jupyter notebook, eliminating the `OpenCV` dependency.

All codes assume the horizontal (typically longer) dimension of the images represent the different  $z$  values sampled at intervals of  $\Delta z$ . Parameters such as the pixel pitch (or spacing/unit cell size)  $z_{\text{pix}}$ —possibly distinct from the pixel *size* quoted on brochures—and estimated tilt angle should be modified if appropriate.

### D. Testing the wavemeter

The red HeNe laser, alongside a cheap and likely multi-mode laser pointer at  $532 \pm 10$ nm green, were each aligned into the wavemeter as described. Because each had a different form factor, alignment was repeated for each. It is unlikely that identical incidence angles were achieved,

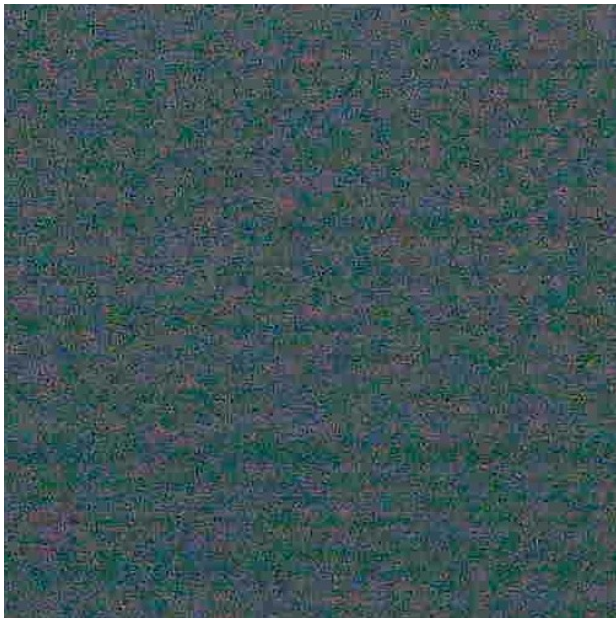


FIG. 9: 500x500 crop of a dark image. Note the fixed pattern noise (lines) and small periodic square artifacts.

but we estimate  $\theta_0$  and  $\phi_0$  to be significantly less than 1 degree. A series of 10 images were captured from each laser, averaged, and then processed.

## V. RESULTS AND DISCUSSION

Generally, the images acquired seemed to reveal the checkerboard-like Talbot patterns, but also exhibited strong and periodic artifacts at the same length scale which interfered with them. All analyses were conducted assuming  $\theta_s = 20.5^\circ$ , estimated by photograph of the `GratingSensorMount` with the sensor board mounted.

### A. Image data

First, a dark frame was captured, where all light was excluded by an opaque foam board. This revealed both typical CMOS fixed-pattern noise and strange blocky artifacts, as shown in Fig. 9. It is unclear whether the latter arise from debayering, compression, or a physical mechanism. These sorts of artifacts persist in the green laser image, Fig. 10, and are joined by clear examples of debayering artifacts in the red laser image, Fig. 12.

### B. Observations and issues

The row-wise Fourier transform of the dark frame, converted to  $z_T$  and then to wavelength, is compared to those of the green laser and the red laser in Fig. 14.

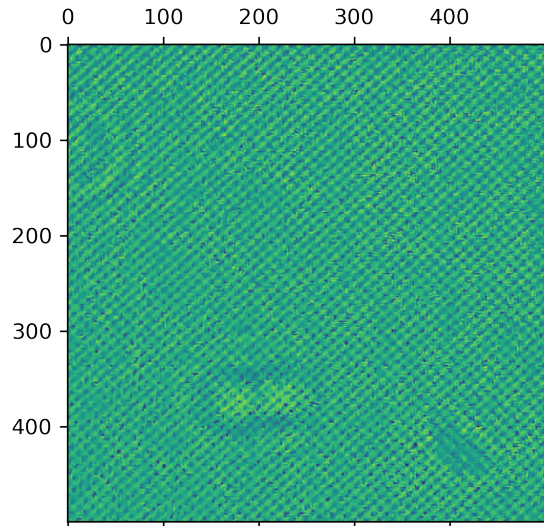


FIG. 10: 500x500 crop of a green image after 10 averages.

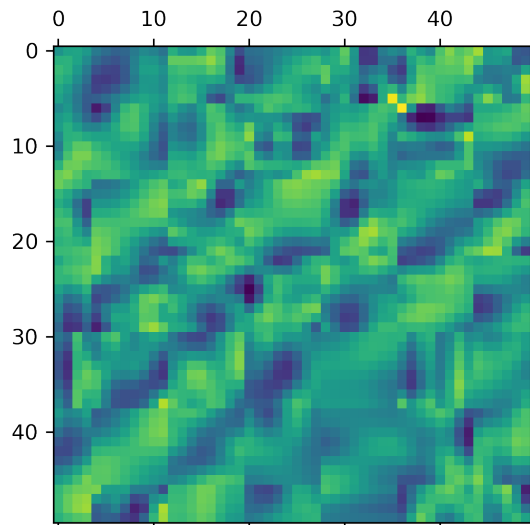


FIG. 11: 50x50 crop of a green image after 10 averages, better displaying the square artifacts.

The numerous peaks appearing in the dark frame are almost certainly not associated with the Talbot pattern. Interestingly, some of these peaks are suppressed when the sensor is exposed to the HeNe, but reappear when the sensor is illuminated by green light. This, and the relatively high visibility of the green laser's Talbot pattern compared to the HeNe's, might be explained by the asymmetry inherent in the sensor's Bayer color filter array between the green pixels and the red/blue pixels. One new peak around nominal 900nm appears in both

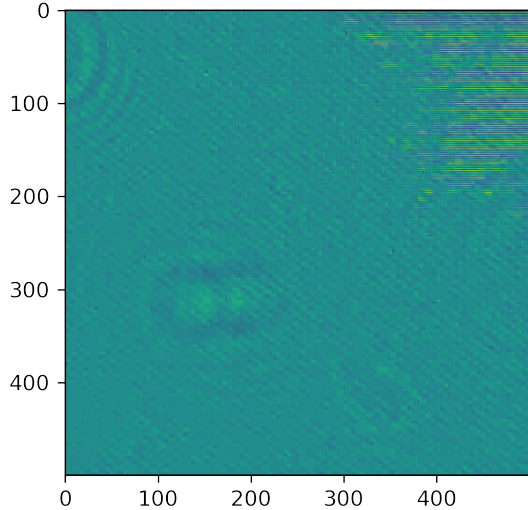


FIG. 12: 500x500 crop of a HeNe image after 10 averages. Note the artifacts in the top right.

the HeNe and green spectra, but not in the dark. This might be due to a spurious reflection, for example within the sensor’s glass filters. The HeNe spectrum apparently contains no unique peaks, which means no wavelength determination can actually be made. The only unique peaks assigned to the green laser, near nominal 200nm and 1150nm, do not correspond to the Talbot pattern’s observed periodicity.

As an additional check for the presence of the Talbot pattern peak, the wavemeter was intentionally misaligned by rotation around the  $y$ -axis of approximately 4 degrees. Observing the Talbot pattern during the rotation showed the expected skew-like transformation. Based on our model of oblique incidence, this should result in splitting of the Talbot peak. However, as shown in Fig. 13, no obvious difference is seen, confirming that the Talbot pattern periodicity is not being effectively extracted.

### C. Next steps

Although further analysis may be able to distinguish the periodic signal due to the Talbot patterns—of which the checkerboard pattern can be discerned by eye in the filtered images—from the other periodic features, the signal-to-noise is poor.

Clearly, more work must be done to acquire clearer Talbot images. To better replicate the original publications, interventions could include using a monochrome sensor to avoid debayering artifacts, improving contrast by better matching the sensor pixel pitch to the grating period, and cutting spurious reflections by removing the protective glass and filters from the sensor. Also, the

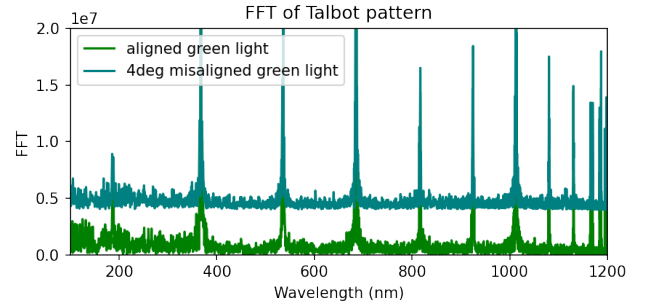


FIG. 13: Wavelengths from measurements on the aligned and 4° misaligned green lasers. They are essentially identical, unlike our model predictions.

raw sensor data should be read without additional image processing, if possible.

At that point, work could proceed on characterizing the empirical performance, in particular the accuracy and drift, of the 3D-printed Talbot wavemeters. Our simulations suggest that this may be futile.

## VI. CONCLUSION

Without a well-functioning prototype, it remains unclear whether the Talbot wavemeter will serve the needs of the OpenQuantum project. We have observed the Talbot pattern via direct sampling by an image sensor, as described in the original publications. These could be vastly improved by adopting measures from said publications. However, the expected performance of the Talbot effect wavemeter, in particular its calculated sensitivity to geometry such as incidence direction and sensor rotation, combined with the difficulty of determining whether normal incidence was achieved within the tolerances required, presents challenges. Although we have no doubt the 10pm resolution claimed in [1] is achievable, the accuracy and stability against drift, affected by the aforementioned issues, has not been characterized. In its current state it appears unlikely that accuracy and consistency will be adequate without significant engineering efforts.

### Acknowledgments and Evaluation

Apologies to the reader for how inefficiently worded this report is. Hopefully someday I’ll clean it up. On the day the paper was due, I rebuilt the apparatus, then retook, reprocessed, and made new plots for all of my data and made major changes to the paper, after suddenly realizing that a major unnoticed error in the wavemeter’s assembly prevented me from observing the checkerboard Talbot patterns in the first place.

I’d like to thank Max Shirokawa Aalto for proposing this project and supporting the hardware side of it, and then finally gathering from a reliable source that the

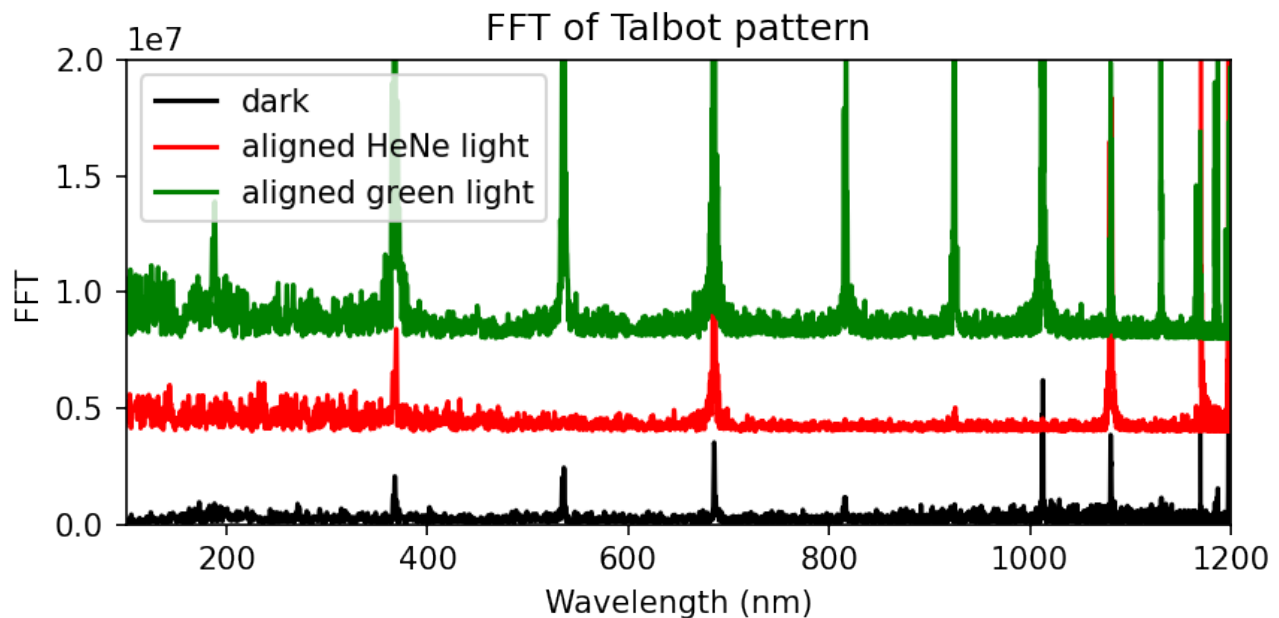


FIG. 14: Wavelengths corresponding to the measured  $z_T$  of dark frame compared to illumination by 532nm green light and the 632.8nm HeNe. Note the many spurious peaks.

Talbot wavemeters “are a bit like the speckle-pattern wavemeters that were published in Nature Comms at one point. A lot of smoke and BS; any kind of perturbation (air movement, temperature change, creep, pressure, ...) will change the interference so much that calling it a wavemeter is nonsense.” According to Max, the reality probably lies somewhere in between. Regardless of the ultimate viability, this has taught me basic things about doing optics in real life. I’d also like to thank Donnie Keathley and professor Dirk Englund for their input and numerous suggestions. And last, but not least, thanks to Isaac Harris for his uncanny ability to find solutions to

optomechanical problems I ran into.

We’re asked to provide a self- and team evaluation discussing what work and writing was done by who. I was a team of one, so these are the same. All aspects of the work were executed by me, with the aid of the aforementioned folks at each step. This includes code, writing, and the experimental setup. The CAD is a modified version of a model designed by one of Max’s colleagues, removing the front portion and lens tube section in favor of a tube for use in a kinematic mount, adjusting clearances for the board, and adding features for use with a yet-to-be-designed 3D-printed kinematic mount.

- 
- [1] N. Han, G. N. West, A. H. Atabaki, D. Burghoff, and R. J. Ram, *Optics Letters* **44**, 4187 (2019), ISSN 1539-4794.
  - [2] E. Ye, A. H. Atabaki, N. Han, and R. J. Ram, *Optics Letters* **41**, 2434 (2016), ISSN 1539-4794.
  - [3] L. Rayleigh, *The London, Edinburgh, and Dublin Philosophical Magazine and Journal of Science* **11**, 196 (1881),

ISSN 1941-5990.

- [4] J. E. Harvey and R. N. Pfisterer, *Optical Engineering* **58**, 1 (2019), ISSN 0091-3286.
- [5] N. Han, S. H. Cho, A. H. Atabaki, E. Ye, W. F. Herring-ton, and R. J. Ram (2016).